NANO LETTERS

Letter

pubs.acs.org/NanoLett

Meta-Lens Doublet in the Visible Region

Benedikt Groever, Wei Ting Chen, and Federico Capasso*

Harvard John A. Paulson School of Engineering and Applied Sciences, Harvard University, Cambridge, Massachusetts 02138, United States

Supporting Information

ABSTRACT: Recently, developments in meta-surfaces have allowed for the possibility of a fundamental shift in lens manufacturing—from the century-old grinding technology to nanofabrication—opening a way toward mass producible high-end meta-lenses. Inspired by early camera lenses and to overcome the aberrations of planar single-layered meta-lenses, we demonstrate a compact meta-lens doublet by patterning two metasurfaces on both sides of a substrate. This meta-lens doublet has a numerical aperture of 0.44, a focal length of 342.5 μm, and a field of view of 50° that enables diffraction-limited monochromatic imaging along the focal plane at a wavelength of 532 nm. The compact design has various imaging applications in microscopy, machine vision, and computer vision.

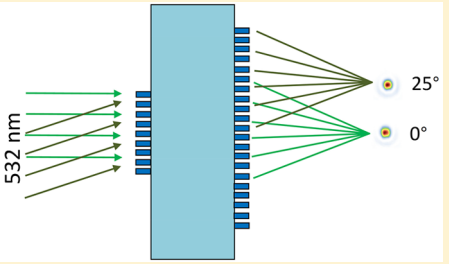

KEYWORDS: *Metasurface, visible wavelength, meta-lens doublet, aberration correction, diffraction-limited*

Even though ancient Greeks had primitive singlet lenses, it was not until the 16th century in Holland that for the first time two different lenses were combined to image an object.[1] A singlet planar lens cannot achieve diffraction-limited focusing for different angles of incidence.[2] This can be solved by adding lenses and therefore provide more degrees of freedom to correct for spherical aberration, coma aberration, astigmatism, and Petzval field curvature.[3,4] However, this solution, combined with conventional lens manufacturing techniques, results in bulky imaging systems.

In recent years, metasurfaces have emerged as a new way of controlling light through the optical properties of subwavelength structures patterned on a flat surface.[5−7] The subwavelength structures are designed to locally change the amplitude, polarization, and phase of an incident beam so that various optical devices can be realized in a compact configuration.[8−20] This becomes important as the demand for portable and wearable devices increases. Here, metasurfaces enable flat optics with new opportunities—especially for compact camera modules.[21−26] Recently, a near diffraction-limited meta-lens doublet in the near-infrared has been demonstrated.[27] To achieve better spatial resolution and for more possible applications, we present, in the visible, a meta-lens doublet showing diffraction-limited focusing along the focal plane for an incidence angle up to 25°. The design builds up on our previous works and corrects for the first time Petzval field curvature, coma aberration, and other monochromatic aberrations in the visible region.[28,29]

The meta-lens doublet presented in this paper is based on the principle of the Chevalier Landscape lens.[30] It was the first widely used camera lens introduced after the invention of the photographic process based on film. Both the Chevalier Landscape lens and our meta-lens doublet have in common a smaller aperture in front of a focusing lens.[31] In the Landscape lens, the rays in normal and oblique incidence are separated by the small aperture and then focused by different parts of the lens so that one can tailor its curvature to reduce aberrations, especially coma aberrations. In our case, the role of the aperture is replaced by an aperture with a metasurface (refer to aperture meta-lens hereafter).

Figure 1a shows a schematic of our meta-lens doublet. An incident beam passes through the aperture meta-lens and substrate before being focused by the focusing meta-lens. The meta-lenses are comprised of titanium dioxide (TiO_2) nanofins with the same length (L), width (W), and height (H) but different rotations arranged on a hexagonal lattice (Figure 1b).[20] Figure 1c−d shows the dimensions of each nanofin. A phase profile $\varphi(x, y)$ is imparted through the rotations of nanofins based on the principles of Berry phase.[32,33] Each nanofin is designed as a half-wave phase shifter converting the incident circularly polarized light into its orthogonal polarization state. The relations between $\varphi(x, y)$ and rotation angles $\alpha(x, y)$ follows: $\varphi(x, y) = 2\alpha(x, y)$, for the case of left-handed circularly polarized (LCP) light (Figure 1e). The phase of the aperture meta-lens was chosen as follows:

$$\varphi_{AL}(x, y) = \sum_{n=1}^{5} a_n \left(\frac{\rho}{R_{AL}}\right)^{2n} \quad (1)$$

and similarly, for the focusing meta-lens:

$$\varphi_{FL}(x, y) = -\frac{2\pi}{\lambda_d}\left(\sqrt{x^2 + y^2 + f^2} - f\right) + \sum_{n=1}^{5} b_n \left(\frac{\rho}{R_{FL}}\right)^{2n} \quad (2)$$

Received: May 5, 2017
Revised: June 26, 2017
Published: June 29, 2017

DOI: 10.1021/acs.nanolett.7b01888
Nano Lett. 2017, 17, 4902−4907

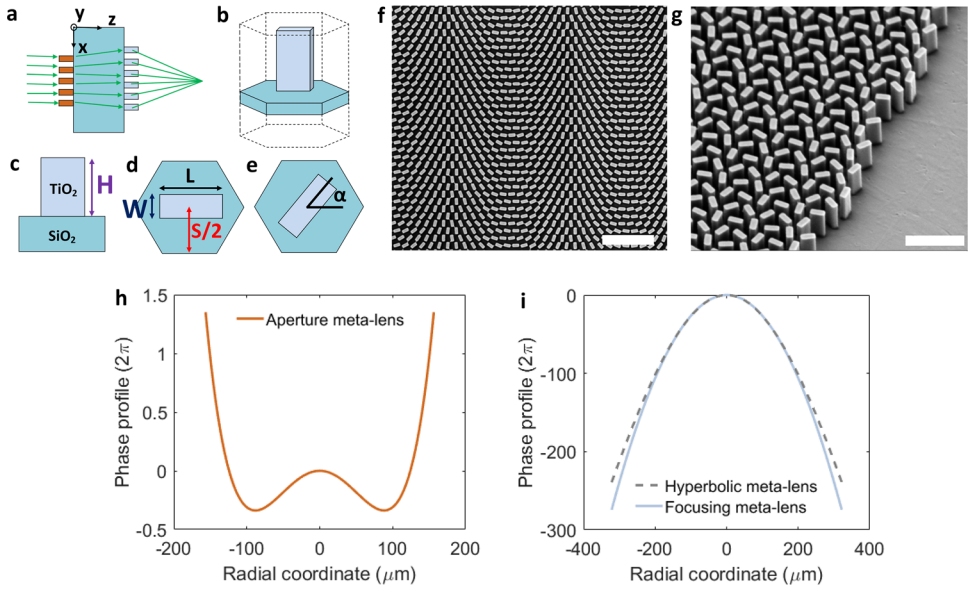

Figure 1. Design, phase profiles, and the scanning electron microscope images of meta-lens doublet. (a) A schematic of the meta-lens doublet. The meta-lens doublet comprises two meta-lenses: aperture meta-lens (depicted in orange) and focusing meta-lens (depicted in light blue) patterned on both sides of a 0.5 mm-thick glass substrate, each meta-lens consists of an array of nanofins with different rotation angles. (b–e) Geometric parameters of the nanofin. The nanofins are arranged in a hexagonal unit cell. (c–e) Side and top views of the hexagonal unit cell. The nanofin dimensions are W = 95, L = 250, H = 600, and S = 320 nm. (f) Top-side view SEM micrograph of the focusing meta-lens. Scale bar: 2000 nm. (g) Side-view SEM micrograph at the edge of the focusing meta-lens. Scale bar: 1000 nm. (h) Phase profile of the aperture meta-lens to correct positive and negative spherical aberrations. (i) A comparison for the phase profile of focusing meta-lens and hyperbolic meta-lens.

Here, λ_d is the design wavelength (= 532 nm), f is the focal length (= 342.3 μm), $\rho = \sqrt{x^2 + y^2}$ is the radial coordinate, x and y are position coordinates of each nanofin with respect to an origin at the center of each lens, and R_{AL} and R_{FL} are the radii of the aperture and focusing meta-lens, respectively. In eq 2, we added a polynomial onto the hyperbolic phase profile to correct aberrations. The coefficients a_n and b_n are optimization parameters. The ray tracing optimization is based on gradient descent with the largest focal spot along the focal plane as objective function. For first optimization step, the initial conditions for a_n and b_n were chosen as $a_n = 0$, $b_n = 0$, for all n. After multiple cycles, the optimization parameters a_n and b_n were obtained such that all rays for various incidence angles up to 25° fall within diffraction-limited Airy disks (see Supporting Tables S1 and S2 for the coefficients).[34] Both aperture meta-lens and focusing meta-lens were fabricated by electron beam lithography followed by atomic layer deposition.[35] They were aligned through alignment marks patterned on both sides of a substrate (see Methods for details). Figure 1f and g shows electron microscope images for the focusing meta-lens. The phase profile of eq 1 and eq 2 were imparted assuming incident LCP and RCP light for the aperture and focusing meta-lens, respectively. The first term of eq 2 shows a hyperbolic shape, and we refer to a meta-lens with this phase profile as hyperbolic meta-lens hereinafter. Figure 1h–i shows the phase plots based on eq 1 and eq 2 for the aperture meta-lens and focusing meta-lens, respectively. We found that the aperture meta-lens has a phase profile similar to a Schmidt plate, which is widely used to correct spherical aberration.[36,37] This phase profile results in converging chief rays and diverging marginal rays. The phase profile of the focusing meta-lens has a stronger phase gradient at the edge than that of the hyperbolic meta-lens (dashed gray line in Figure 1i, plotted with the first term of eq 2 only).

Figure 2a shows the ray diagram for the hyperbolic meta-lens, which is only capable of achieving diffraction-limited focusing at normal incidence. The inset shows a magnified plot of the rays near the focal plane. At oblique incidences, it suffers strong aberrations; we found that this cannot be corrected by adding another metasurface as a correcting lens without modifying its hyperbolic phase profile, because the ray diagrams for different angles of incidence are significantly different. Figure 2b shows the case for the focusing meta-lens without the aperture meta-lens. The focusing meta-lens has the same design parameter as the meta-lens doublet. Through the stronger phase gradient at the edge (see light blue curve in Figure 1i) compared to that of the hyperbolic meta-lens, the marginal rays get bent more toward the optical axis (focusing before the focal plane), while chief rays get bent less (focusing behind the focal plane). These effects are known as positive and negative spherical aberrations, respectively. The phase profile of the focusing meta-lens results in similar ray diagrams (Figure 2b) for different incidence angles and therefore provides a possibility to correct the aberrations. In Figure 2c, with the aperture meta-lens, the positive and negative spherical aberrations are corrected to realize diffraction-limited focusing along the focal plane. Figure 2d shows an analog ray diagram with refractory lenses. Spherical aberrations are corrected by the Schmidt plate in such a way that marginal rays are diverged, which increases the "effective focal length", while chief rays are converged, which decreases the "effective focal length".

Figure 3a shows a schematic setup for measuring the size of the focal spot for different angles of incidence. An objective of NA = 0.95 with a tube lens (f = 180 mm) is used to magnify the focal spot by 100 times on a camera with a pixel size of 2.2 μm. The sample, objective, tube lens, and camera are mounted on a rail to adjust the angle of incidence. The light source is a λ = 532 nm laser with a bandwidth of 30 GHz (28 pm), which means that chromatic aberrations can be neglected. For the

DOI: 10.1021/acs.nanolett.7b01888
Nano Lett. 2017, 17, 4902–4907

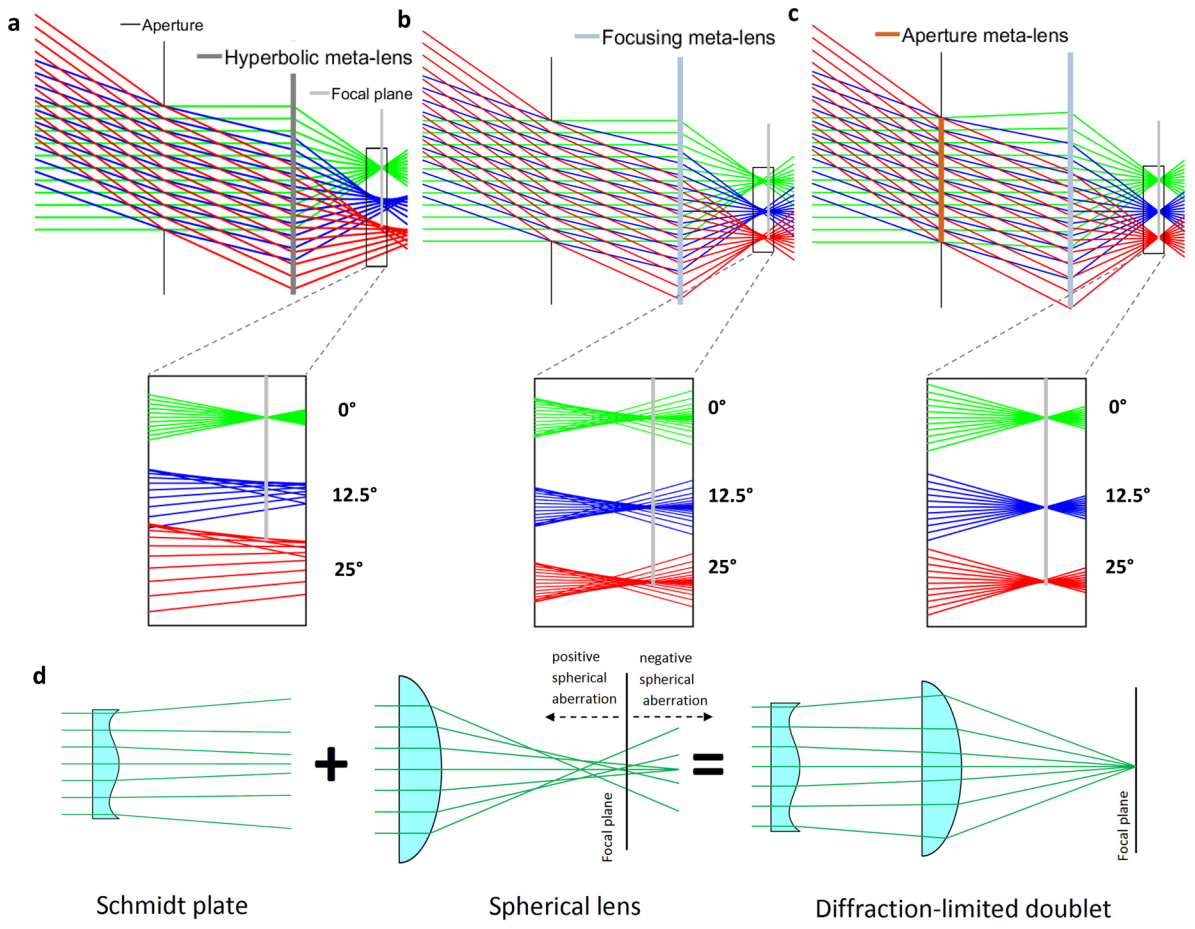

Figure 2. Ray diagrams for explaining the principle of aberration correction. (a) Ray diagram of a meta-lens with hyperbolic phase profile showing large aberrations at oblique incidence. (b) Ray diagram of the focusing meta-lens with phase profile shown in the light blue curve in Figure 1i. (c) Ray diagram obtained by adding the aperture meta-lens resulting in diffraction-limited focusing along the focal plane. The insets of panels a–c show the magnified plots near their focal planes. (d) Analog of refractive lenses: The operation of the meta-lens doublet in terms of the correction of spherical aberration is analogous to that of a Schmidt plate combined with a spherical lens. The positive and negative spherical aberrated marginal and chief rays are corrected through the concave and convex curvature of the Schmidt plate.

measurement, we illuminated the full diameter of the aperture meta-lens. Figure 3b–f shows the focal spots for an incidence angle up to 25°. Slightly asymmetric sidelobes result from the misalignment of aperture and focusing meta-lens. Through the comparison of measured and simulated focal spots (Supporting Figure S1), we estimate that the misalignment between the meta-lenses is about a few micrometers. The misalignment need to be controlled below 10 μm to ensure diffraction-limited focusing. Figure 3g shows the full-widths at half-maximum (fwhm's) $\sim\frac{\lambda_d}{2NA}$ for all incidence angles up to 25°. Their Strehl ratios are approximately equal to or larger than 0.8 (Supporting Figure S2), which meets the requirement of diffraction-limited focusing.[38] Slight deviations arise from small misalignments between the two meta-lenses and finite camera pixel size. Figure 3h shows the diffraction-limited modulation transfer function MTF for different incidence angles. We obtained the MTF by taking the modulus of the discrete Fourier transformation of the intensity distribution at the intersection between the focal plane and the plane of incidence ($\hat{x}$ direction in Figure 3a). In general, the MTF value drops for large spatial frequencies with a cutoff frequency of $\frac{2NA}{\lambda_d}$. The resolution limit of an imaging system is defined by the inverse of the spatial frequency at which the MTF has a value of 0.1. Lowering the NA and cascading more metasurfaces with properly placed entrance and exit apertures can further increase the field of view.[39] Simulated focal spots with incidence angles beyond 25° are provided in Figure S3 for reference.

Subsequently, we used this meta-lens for widefield imaging. Figure 4 shows the schematic setup for imaging the 1951 US Air Force resolution target. The target is placed at the focal plane and then imaged through the meta-lens doublet (Figure 4a). To reduce laser speckle, a supercontinuum laser (SuperK, NKT Inc.) with 5 nm bandwidth is used. The resolution target consists of stripe groups: each group contains three vertical and horizontal bars with an equal line width and gap. Here we image the group with a line width of ~2.2 μm. From Figure 4b–h, we move our meta-lens doublet in steps of 25.4 μm away from the optical axis to characterize image quality; this corresponds to different fields of view of the meta-lens doublet. The largest movement ~152 μm (Figure 4h) corresponds to a diffraction angle equal to ~25°; the horizontal bars become blurred because chromatic aberration becomes more significant at larger angles (Supporting Figures S4–S5).

Figure 5a–j shows the images when we place the target at the center of the meta-lens doublet in normal incidence. Figure 5a–f shows the images taken using a tunable laser as light source with a center wavelength at 532 nm of various

DOI: 10.1021/acs.nanolett.7b01888
Nano Lett. 2017, 17, 4902–4907

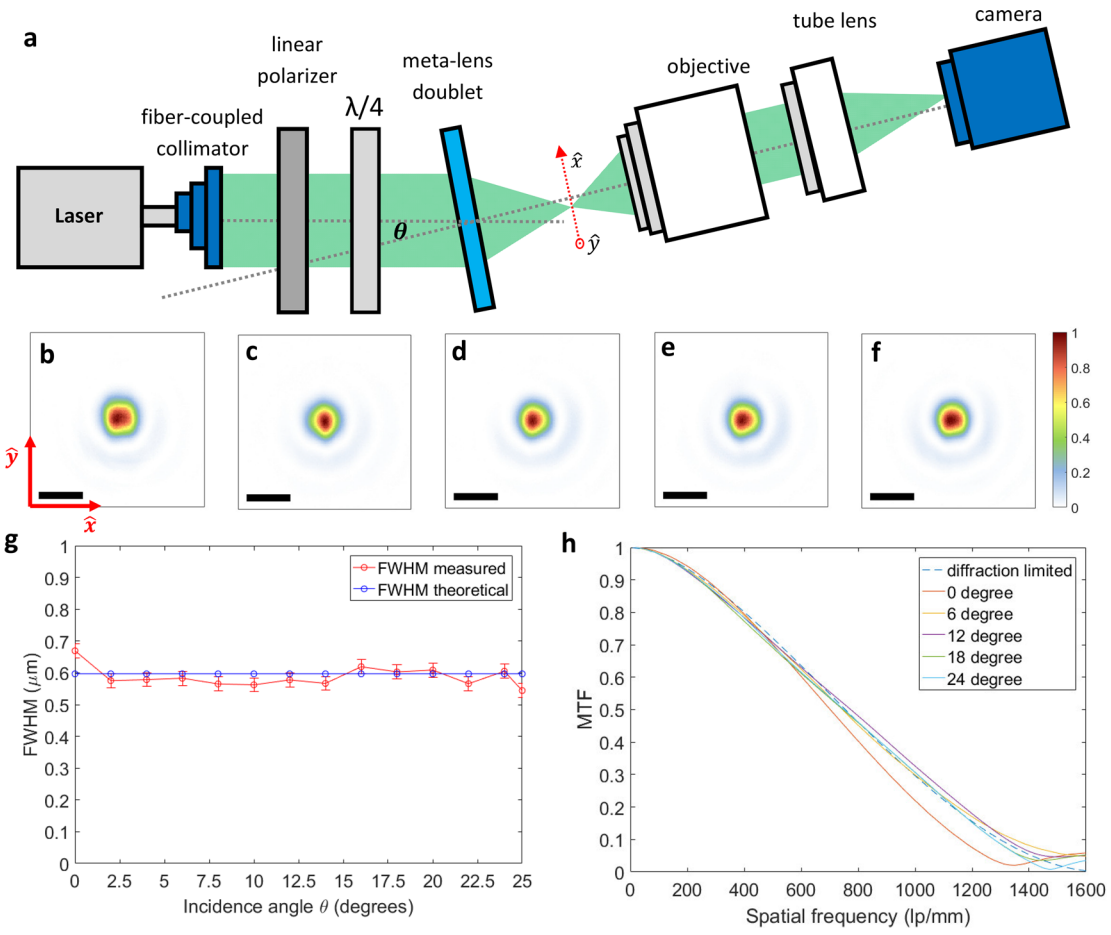

Figure 3. Focal spot characterization for different angles of incidence (θ) at λ_d = 532 nm. (a) Focal spot measurement setup. (b–f) Focal spot intensity profile at (b) 0°, (c) 6°, (d) 12°, (e) 18°, (f) 25° incidence angle θ. Scale bar: 1.1 μm. Their fwhm's along the $\hat{x}$ direction are shown in panel g in comparison to modeling. (h) Measured modulation transfer function (MTF) curve along the $\hat{x}$ direction at different incidence angles. The horizontal axis is in units of line pair per millimeter. A diffraction-limit MTF curve (blue dashed line) is provided as a reference.

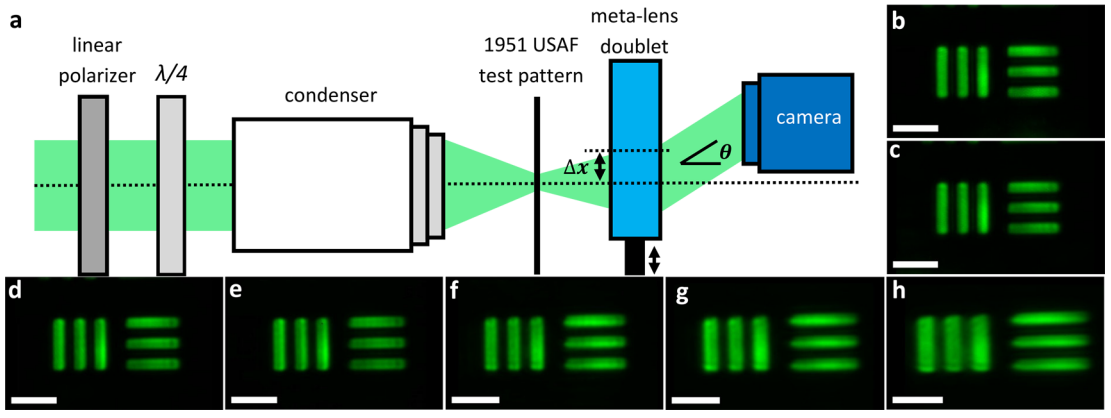

Figure 4. Imaging with the meta-lens doublet for the element 6 in group 7 of 1951 US air force resolution target: 2.2 μm line width and gap. (a) Imaging setup using meta-lens doublet. The illumination light source is from a laser centered at 532 nm with a bandwidth of 5 nm. (b–h) Images taken by moving the meta-lens doublet 25.4 μm per step with respect to the center of the target. Each movement, Δx, corresponds to an angle θ. Scale bar: 11 μm. The (Δx, θ) from b to h are (0 μm, 0°), (25.4 μm, 4.11°), (50.8 μm, 8.26°), (76.2 μm, 12.48°), (101.6 μm, 16.83°), (127 μm, 21.33°), and (152.4 μm, 26.05°).

bandwidths from 5 to 100 nm, while Figure 5g–j shows that of difference center wavelengths with a constant 5 nm bandwidth. In Figure 5f, although the feature can still be resolved, the contrast drops significantly when the laser bandwidth increase is increased to 100 nm. This represents a drop in the MTF value as shown in Figure 5k, which results from chromatic aberration: focal length changes with wavelength (Figure 5l). The chromatic aberration can be reduced by several approaches: refractive/diffractive compound lens,[40] dispersion engineering of nanostructure resonances,[41,42] or designing a nanostructure that can provide more than 2π phase modulation.[43−45] Even though the meta-lens doublet is

DOI: 10.1021/acs.nanolett.7b01888
Nano Lett. 2017, 17, 4902−4907

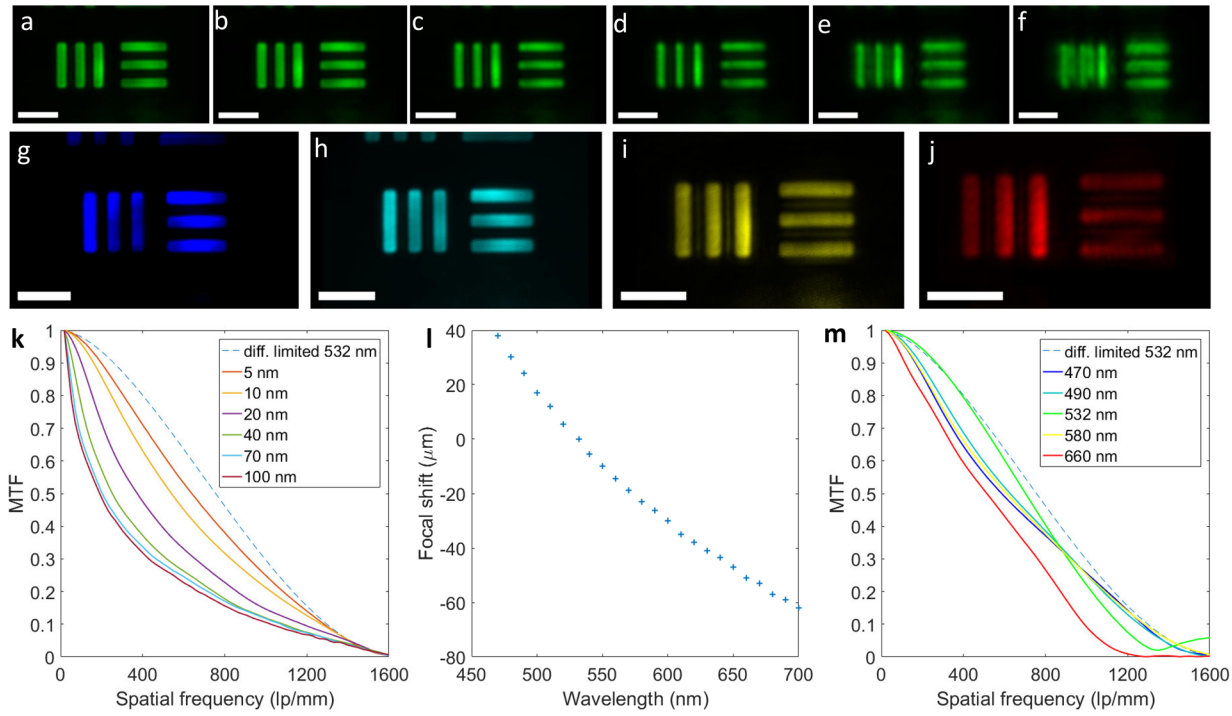

Figure 5. Analysis of the chromatic properties of the meta-lens doublet. (a–f) On-axis imaging at normal incidence with laser center wavelength λ = 532 nm and a bandwidth of (a) 5 nm, (b) 10 nm, (c) 20 nm, (d) 40 nm, (e) 70 nm, (f) 100 nm. Scale bar: 11 μm. (g–j) On-axis imaging with a laser bandwidth of 5 nm and a center wavelength at (g) 470 nm, (h) 490 nm, (i) 580 nm, and (j) 660 nm. Scale bar: 11 μm. (k) MTF for different bandwidths at 532 nm in normal incidence. (l) Chromatic focal length shift of the meta-lens doublet as a function of wavelength. Reference is the focal length at designed wavelength λ_d = 532 nm. (m) MTF for different laser center wavelengths with a 5 nm bandwidth.

designed at 532 nm, it is still capable of resolving the target clearly at other wavelengths with 5 nm bandwidth. Figure 5m shows the MTF curve as a quantitative analysis of Figure 5g–j. Also notable, the meta-lens doublet has low temperature dependence from 25 to 70 °C. Its focal spot remains diffraction-limited (Supporting Figure S6). The maximum focusing efficiency of the meta-lens doublet is about 50% (Supporting Figure S7).

In conclusion, we have demonstrated a meta-lens doublet consisting of nanofins at wavelength λ_d = 532 nm, with a numerical aperture of 0.44, a focal length of 342.3 μm, and 50° field of view. The meta-lens doublet is not only capable of performing diffraction-limited focusing, but also can realize high quality imaging along the focal plane. Unlike in traditional Fresnel lenses, the use of nanostructures can provide another degree of freedom to engineer the chromatic aberration. In addition, meta-lens doublets can be mass produced by deep ultraviolet lithography or nanoimprinting. The meta-lens doublet can find many applications in laser-based microscopy and spectroscopy as well as in computer vision and machine vision.

Methods. The details of the fabrication can be found in Supporting Note 1.

The measurement setup includes a super continuum laser (NKT SuperK) equipped with an tunable filter (NKT Varia) with a fiber output. A narrowband green laser (Laser Quantum, Ventus532) with a bandwidth of 30 GHz ~ 28 pm was selectively used. The incident beam was collimated by a fiber collimator (RC12APC-P01, Thorlabs) and then circularly polarized through a wire grid polarizer (Thorlabs WP25L-UB) followed by a quarter wave plate (Thorlabs AQWP05M-600). The focal size is magnified by an objective (Olympus, MPLAPON, 100×, NA = 0.95) paired with a tube lens (Thorlabs, AC508–180-A-ML), then imaged on a monochromatic camera (Edmund Optics, EO-5012). Images of the resolution target were taken with another camera (Thorlabs, DCC1545M).

■ ASSOCIATED CONTENT

Supporting Information

The Supporting Information is available free of charge on the ACS Publications website at DOI: 10.1021/acs.nanolett.7b01888.

Figures S1–S7 and Supporting Note 1: Fabrication of the meta-lens doublet (PDF)

■ AUTHOR INFORMATION

Corresponding Author

*E-mail: capasso@seas.harvard.edu.

ORCID

Benedikt Groever: 0000-0002-8020-4737

Wei Ting Chen: 0000-0001-8665-9241

Notes

The authors declare no competing financial interest.

■ ACKNOWLEDGMENTS

This work was supported by the Air Force Office of Scientific Research (MURI, grant no. FA9550-14-1-0389 and grant no. FA9550-16-1-0156). This work was performed in part at the Center for Nanoscale Systems (CNS), a member of the National Nanotechnology Coordinated Infrastructure (NNCI), which is supported by the National Science Foundation under NSF award no. 1541959. CNS is part of Harvard University.

DOI: 10.1021/acs.nanolett.7b01888
Nano Lett. 2017, 17, 4902–4907

Federico Capasso gratefully acknowledges a gift from Huawei Inc. under its HIRP FLAGSHIP program. The authors acknowledge Dr. Mohammadreza Khorasaninejad for his support in FDTD simulation and Mr. Ameha Gebreyohannes for his support in fabrication.

REFERENCES

(1) King, H. C. *The history of the telescope*; Courier Corporation, 1955.
(2) Aieta, F.; Genevet, P.; Kats, M. A.; Yu, N.; Blanchard, R.; Gaburro, Z.; Capasso, F. *Nano Lett.* **2012**, *12* (9), 4932−4936.
(3) Gross, H.; Zugge, H.; Peschka, M.; Blechinger, F. *Handbook of Optical Systems: Vol. 3. Aberration Theory and Correction of Optical Systems*; Wiley: New York, 2007.
(4) Strojnik, M.; Paez, G.; Malacara, D.; Thompson, B. *Handbook of Optical Engineering*; Marcel Dekker: New York, 2001.
(5) Yu, N.; Genevet, P.; Kats, M. A.; Aieta, F.; Tetienne, J.-P.; Capasso, F.; Gaburro, Z. *Science* **2011**, *334* (6054), 333−337.
(6) Yu, N.; Capasso, F. *Nat. Mater.* **2014**, *13* (2), 139−150.
(7) Kildishev, A. V.; Boltasseva, A.; Shalaev, V. M. *Science* **2013**, *339* (6125), 1232009.
(8) Chen, W. T.; Török, P.; Foreman, M.; Liao, C. Y.; Tsai, W.-Y.; Wu, P. R.; Tsai, D. P. *Nanotechnology* **2016**, *27* (22), 224002.
(9) Chen, W. T.; Yang, K. Y.; Wang, C. M.; Huang, Y. W.; Sun, G.; Chiang, I. D.; Liao, C. Y.; Hsu, W. L.; Lin, H. T.; Sun, S.; Zhou, L.; Liu, A. Q.; Tsai, D. P. *Nano Lett.* **2014**, *14* (1), 225−230.
(10) Groever, B.; Heshmat, B.; Raskar, R. *ACS Photonics* **2016**, *3* (6), 930−935.
(11) Sun, S.; Yang, K.-Y.; Wang, C.-M.; Juan, T.-K.; Chen, W. T.; Liao, C. Y.; He, Q.; Xiao, S.; Kung, W.-T.; Guo, G.-Y.; Zhou, L.; Tsai, D. P. *Nano Lett.* **2012**, *12* (12), 6223−6229.
(12) Hao, J.; Yuan, Y.; Ran, L.; Jiang, T.; Kong, J. A.; Chan, C.; Zhou, L. *Phys. Rev. Lett.* **2007**, *99* (6), 063908.
(13) Huang, L.; Chen, X.; Mühlenbernd, H.; Li, G.; Bai, B.; Tan, Q.; Jin, G.; Zentgraf, T.; Zhang, S. *Nano Lett.* **2012**, *12* (11), 5750−5755.
(14) Kawata, S.; Sun, H.-B.; Tanaka, T.; Takada, K. *Nature* **2001**, *412* (6848), 697−698.
(15) Liu, X.; Galfsky, T.; Sun, Z.; Xia, F.; Lin, E.-c.; Lee, Y.-H.; Kéna-Cohen, S.; Menon, V. M. *Nat. Photonics* **2014**, *9* (1), 30−34.
(16) Luk'yanchuk, B.; Zheludev, N. I.; Maier, S. A.; Halas, N. J.; Nordlander, P.; Giessen, H.; Chong, C. T. *Nat. Mater.* **2010**, *9* (9), 707−715.
(17) Valentine, J.; Zhang, S.; Zentgraf, T.; Ulin-Avila, E.; Genov, D. A.; Bartal, G.; Zhang, X. *Nature* **2008**, *455* (7211), 376−379.
(18) Mueller, J. B.; Rubin, N. A.; Devlin, R. C.; Groever, B.; Capasso, F. *Phys. Rev. Lett.* **2017**, *118* (11), 113901.
(19) Plum, E.; Zhou, J.; Dong, J.; Fedotov, V.; Koschny, T.; Soukoulis, C.; Zheludev, N. *Phys. Rev. B: Condens. Matter Mater. Phys.* **2009**, *79* (3), 035407.
(20) Krishnamoorthy, H. N.; Jacob, Z.; Narimanov, E.; Kretzschmar, I.; Menon, V. M. *Science* **2012**, *336* (6078), 205−209.
(21) Arbabi, A.; Horie, Y.; Ball, A. J.; Bagheri, M.; Faraon, A. *Nat. Commun.* **2015**, *6*, 7069.
(22) Arbabi, A.; Horie, Y.; Bagheri, M.; Faraon, A. *Nat. Nanotechnol.* **2015**, *10* (11), 937−943.
(23) Chen, W. T.; Khorasaninejad, M.; Zhu, A. Y.; Oh, J.; Devlin, R. C.; Zaidi, A.; Capasso, F. *Light: Sci. Appl.* **2016**, *14*, 0.
(24) Lin, D.; Fan, P.; Hasman, E.; Brongersma, M. L. *Science* **2014**, *345* (6194), 298−302.
(25) Rogers, E. T.; Lindberg, J.; Roy, T.; Savo, S.; Chad, J. E.; Dennis, M. R.; Zheludev, N. I. *Nat. Mater.* **2012**, *11* (5), 432−435.
(26) Wood, B.; Pendry, J.; Tsai, D. *Phys. Rev. B: Condens. Matter Mater. Phys.* **2006**, *74* (11), 115116.
(27) Arbabi, A.; Arbabi, E.; Kamali, S. M.; Horie, Y.; Han, S.; Faraon, A. *Nat. Commun.* **2016**, *7*, 13682.
(28) Khorasaninejad, M.; Chen, W. T.; Devlin, R. C.; Oh, J.; Zhu, A. Y.; Capasso, F. *Science* **2016**, *352* (6290), 1190−1194.
(29) Khorasaninejad, M.; Chen, W. T.; Oh, J.; Capasso, F. *Nano Lett.* **2016**, *16* (6), 3732−3737.
(30) Kingslake, R. *A history of the photographic lens*; Elsevier, 1989.
(31) Buralli, D. A.; Morris, G. M. *Appl. Opt.* **1989**, *28* (18), 3950−3959.
(32) Berry, M. V. *J. Mod. Opt.* **1987**, *34* (11), 1401−1407.
(33) Pancharatnam, S. *S. Proc. Indian Acad. Sci.* **1956**, *44* (5), 247−262.
(34) Bociort, F. *Encyclopedia of Optical Engineering* **2003**, *2*, 1843−1850.
(35) Devlin, R. C.; Khorasaninejad, M.; Chen, W. T.; Oh, J.; Capasso, F. *Proc. Natl. Acad. Sci. U. S. A.* **2016**, *113* (38), 10473−10478.
(36) Johnson, T. J. Method for making replica contour block masters for producing schmidt corrector plates. U.S. Patent US3837124 A, 1974.
(37) Johnson, T. J. Method for making schmidt corrector lenses. U.S. Patent US3889431 A, 1975.
(38) Thorlabs Super Apochromatic Mircoscope Objectives. https://www.thorlabs.com/newgrouppage9.cfm?objectgroup_id=9895 (June 18, 2017).
(39) Geary, J. M. *Introduction to Lens Design*; Willmann-Bell, 2002.
(40) Stone, T.; George, N. *Appl. Opt.* **1988**, *27* (14), 2960−2971.
(41) Faklis, D.; Morris, G. M. *Appl. Opt.* **1995**, *34* (14), 2462−2468.
(42) Sweeney, D. W.; Sommargren, G. E. *Appl. Opt.* **1995**, *34* (14), 2469−2475.
(43) Lin, J.; Mueller, J. P. B.; Wang, Q.; Yuan, G.; Antoniou, N.; Yuan, X.-C.; Capasso, F. *Science* **2013**, *340* (6130), 331−334.
(44) Aieta, F.; Kats, M. A.; Genevet, P.; Capasso, F. *Science* **2015**, *347* (6228), 1342−1345.
(45) Khorasaninejad, M.; Shi, Z.; Zhu, A.; Chen, W. T.; Sanjeev, V.; Capasso, F. *Nano Lett.* **2017**, *17* (3), 1819−1824.

DOI: 10.1021/acs.nanolett.7b01888
Nano Lett. 2017, 17, 4902−4907